Coherence function-encoded optical palpation

QI FANG,[1,2,*] PHILIP WIJESINGHE,[1,2,3] RHYS JONES,[1,4] DEVINA D. LAKHIANI,[1,2] BENJAMIN F. DESSAUVAGIE,[5,6] BRUCE LATHAM,[5,7] CHRISTOBEL M. SAUNDERS,[8,9,10] AND BRENDAN F. KENNEDY[1,2,11]

[1]BRITElab, Harry Perkins Institute of Medical Research, QEII Medical Centre, Nedlands and Centre for Medical Research, The University of Western Australia, Crawley, Western Australia, 6009, Australia
[2]Department of Electrical, Electronic & Computer Engineering, School of Engineering, The University of Western Australia, Crawley, Western Australia, 6009, Australia
[3]Currently with SUPA, School of Physics and Astronomy, University of St Andrews, North Haugh, St Andrews KY16 9AJ, United Kingdom
[4]Currently with University of Melbourne, Parkville, Victoria, 3010, Australia
[5]PathWest, Fiona Stanley Hospital, 11 Robin Warren Drive, Murdoch, Western Australia, 6150, Australia
[6]School of Pathology and Laboratory Medicine, The University of Western Australia, Crawley, Western Australia, 6009, Australia
[7]The University of Notre Dame, Fremantle, Western Australia, 6160, Australia
[8]Division of Surgery, Medical School, The University of Western Australia, Crawley, Western Australia, 6009, Australia
[9]Breast Centre, Fiona Stanley Hospital, 11 Robin Warren Drive, Murdoch, Western Australia, 6150, Australia
[10]Breast Clinic, Royal Perth Hospital, 197 Wellington Street, Perth, Western Australia, 6000, Australia
[11]Australian Research Council Centre for Personalised Therapeutics Technologies, Australia
**Corresponding author: qi.fang@uwa.edu.au*

Optical palpation can map stress at the surface of biological tissue into 2-D images. It relies on measuring surface deformation of a compliant layer, which to date has been performed with optical coherence tomography (OCT). OCT-based optical palpation holds promise for improved clinical diagnostics, however, the complexity and cost may hinder broad adoption. In this Letter, we introduce coherence function-encoded optical palpation (CFE-OP) using a novel optical profilometry technique that exploits the envelope of the coherence function rather than its peak position which is typically used to retrieve depth information. CFE-OP utilizes a Fabry-Pérot laser diode (bandwidth, 2.2 nm) and a single photodiode in a Michelson interferometer to detect the position along the coherence envelope as a function of path length. This technique greatly reduces complexity in comparison to the OCT-based approach, promising rapid and low-cost optical palpation. We perform CFE-OP on both a phantom and excised human breast tissue, demonstrating comparable mechanical contrast to OCT-based optical palpation and the capability to distinguish stiff tumor from soft benign tissue.

Optical palpation [1] is a technique that mimics the clinician's sense of touch by mapping stress applied to the surface of biological tissues. It utilizes an optical imaging technique to measure deformation (strain) introduced to a compliant layer placed in contact with tissue. By relating the measured strain to the pre-characterized stress-strain response of the compliant layer, a 2-D stress map is generated. Due to its uncomplicated working principle and the potential to incorporate the technique in imaging probes, optical palpation has been proposed for clinical applications such as tumor margin assessment in breast-conserving surgery [2] and *in vivo* scar assessment [3].

Optical palpation has mainly been implemented with optical coherence tomography (OCT) [1-3], with several recent techniques also demonstrating optical palpation based on digital cameras [4, 5]. Although OCT implementations have successfully demonstrated tumor detection on breast specimens and scar treatment assessment on skin, they comprise complex and expensive optical components, such as low-noise broadband light sources and high-resolution spectrometers, hindering the widespread use of optical palpation in clinical settings. In addition, OCT-based optical palpation acquires 3-D OCT images, whilst only a 2-D depth map of the stress sensor surface is generated [1]. Acquisition of 3-D data limits the imaging rate, resulting in degradation of image quality when using handheld imaging probes, as the frequency of hand motion often exceeds the data acquisition rate [6]. Extracting 2-D depth maps from 3-D data sets also increases the data processing burden, further complicating the real-time use of optical palpation in clinical scenarios.

In this Letter, we propose a more practical and cost-effective optical palpation system, termed coherence function-encoded optical palpation (CFE-OP), than other stress mapping techniques, such as OCT-based optical palpation and atomic force microscopy. Our technique can generate 2-D stress maps at the tissue surface based on the deformation measurement of a novel compliant layer, using a new optical profilometry technique. Previous interferometry-based optical profilometry techniques [7, 8] utilize low-coherent light sources with short coherence lengths and record the peak position on the coherence function to provide depth

measurements. These techniques require a piezoelectric actuator to scan over the full depth range of the target surface, introducing additional noise from the actuator position measurement and limiting the acquisition rate to the scanning speed of the actuator, typically a few seconds for millimeter-scale distances [9]. In CFE-OP, we introduce a light source with a coherence length on the same scale as the layer thickness. Instead of scanning over the entire depth range, CFE-OP uses a piezoelectric actuator to continuously drive the reference mirror with a small amplitude of ~0.5 μm to create a modulation of the optical path length, and the coherence function amplitude is derived from the maximum and minimum values of the modulated light intensity measured at the interferometer output port. Depth sensing is then realized by characterizing the relationship between the coherence function amplitude, i.e., the position on the coherence function envelope, and the sample arm reflector position. When the surface position of the compliant layer in the sample arm changes due to compression against a tissue surface, the path length between the sample and reference arms also changes, resulting in a variation of the coherence function amplitude that can be directly related to layer surface displacement. Knowing this displacement, stress can be derived through knowledge of the stress-displacement response of the compliant layer. A 2-D stress map of the layer surface can be generated by laterally scanning the beam in two orthogonal directions. This approach enables depth sensing to be performed over a large depth range, without noise introduced by position measurement from the actuator. With this approach, an acquisition rate of 400 Hz over a depth range of ~300 μm was achieved for depth sensing at each lateral pixel location.

In this proof-of-principle study, we first characterize the coherence function as a function of sample arm reflector position relative to the reference mirror. We then demonstrate CFE-OP on a silicone phantom with an embedded stiff inclusion and compare the results with OCT-based optical palpation. Finally, we perform CFE-OP on human breast tissue freshly excised from mastectomy surgery. The tissue results are co-registered with "gold standard" post-operative histology, demonstrating the capability of our technique to distinguish stiff regions of tumor from softer benign tissue.

Figure 1(a) shows a schematic of the experimental setup. A broadband Fabry-Pérot laser diode (Thorlabs, FPL1053S) serves as the light source. The laser diode is connected to a driver (Thorlabs, CLD1015) and the output power is 20 mW. The laser spectrum, as shown in Fig. 1(a), was measured using an optical spectrum analyzer (Agilent, 86140B), where the central wavelength is 1304 nm and the full-width-at-half-maximum (FWHM) bandwidth is 2.2 nm, providing a coherence length of ~340 μm. The coherence function of the laser source, which is the Fourier transform of its optical spectrum, has a Gaussian profile at the central range of ±500 μm. The interferometer comprises a reference arm where the beam is reflected from a reference mirror that is attached to a piezoelectric actuator, and a sample arm where the beam is scanned by a galvanometer-based mirror system with 400 × 400 pixels in a scanning field-of-view of 10×10 mm^2. The scan rate is 1 Hz in the fast axis and 0.0025 Hz in the slow axis. A photodiode records the interference signals at an acquisition rate of 10,000 Hz, from which the coherence function is derived.

Stress measurement in optical palpation is achieved by adding a compliant layer between a flat, transparent imaging window and the tissue [1]. When the layer is compressed against tissue, it deforms due to the reactive stress at its surface. In OCT-based

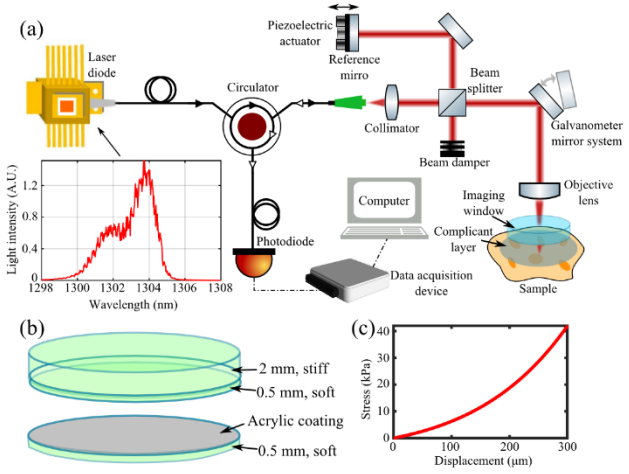

Fig. 1 (a) Schematic of the experimental setup. Inset: measured spectrum of the laser diode. (b) Schematic of the multi-sectional compliant layer. (c) Measured stress-displacement curve of the cured top-middle section of the layer.

optical palpation, the deformation of the compressed layer is obtained using a Canny edge detection algorithm to determine the layer-tissue interface [1]. As the stress-strain curve of the layer is pre-characterized, assuming a uniaxial stress distribution across the layer, 2-D stress maps at the tissue surface can be generated. In CFE-OP, we have developed a customized, multi-sectional compliant layer as shown in the schematic Fig. 1(b). This layer comprises three sections: a stiffer 2 mm thick top section (Wacker RT601 A and B and silicone oil (Wacker, AK 50) at 10:1:10 mixing ratio, tangent modulus = 225.6 ± 11.2 kPa at 20% strain), softer middle and bottom sections of thickness 0.5 mm (Wacker P7676 A and B at 1:1 mixing ratio, tangent modulus = 30.7 ± 1.9 kPa at 20% strain). The top and middle sections are cured together, resulting in a strong bond between them, while the bottom section is cured separately. To increase the signals received by the photodiode, we spray-painted the top surface of the bottom section with a highly reflective acrylic coating by using a fine-nozzle compressed-air sprayer (Voilamart, 0.3 mm diameter nozzle). The soft bottom section is to avoid the acrylic coating directly contacting and contaminating the tissue and the soft middle section is required for the stress measurement. The stiffness of the two soft sections was comparable to that of the sample to allow sufficient contrast in lateral plane in stress maps when compression is applied. The stiff top section was designed to be sufficiently thick to avoid interference from the layer-imaging window interface. In the experiment, the multi-sectional layer was placed on top of the tissue and the coated surface fully contacted with the middle section to avoid any air gaps, so the displacement (deformation) of the highly reflective coated surface can be accurately measured from the position on the coherence function envelope once compressed against the tissue. The stress-displacement curve of the cured top-middle section was pre-characterized using a custom uniaxial compression device where the displacement was read from a motorized *z*-stage and the stress value was derived from the force measured by a load cell [4]. The data was fitted to a double-exponential curve, as shown in Fig. 1(c). By combining the 2-D displacement map of the coated layer surface with the stress-displacement curve, 2-D stress maps of the tissue surface can be generated, assuming uniaxial stress distribution at the layer-tissue interface.

The displacement of the coated layer surface is encoded in the position on the coherence function envelope of the interferometer. The light intensity received by the photodiode is expressed as [10]:

$$I_{PD} = I_R + I_S + 2\sqrt{I_R I_S}\gamma(z)\cos\varphi, \quad (1)$$

where I_R and I_S are intensities of the reflection from the reference and sample arms, respectively. The constant intensity I_R can be measured from the photodiode by blocking the sample arm in the interferometer. In the last term of Eq. (1), the coherence function $\gamma(z)$ is a function of position z of the highly reflective layer surface, assuming its path length is matched to that of the reference mirror at 0% strain of the compliant layer, $\varphi = \frac{4\pi z}{\lambda}$ is the phase difference between the reference and sample arms and λ is the central wavelength of the light source. Assuming a Gaussian spectrum light source, the coherence function is expressed as [11]:

$$\gamma(z) = e^{-(\frac{\pi \Delta\lambda\, z}{\sqrt{ln2}\,\lambda^2})^2}, \quad (2)$$

where $\Delta\lambda$ is the FWHM bandwidth of the light source.

We drove the reference mirror with the piezoelectric actuator with a sinusoidal function. The phase difference in the interference term in Eq. (1) is then a function of time:

$$\varphi(t) = \frac{4\pi}{\lambda}[z + A\sin(2\pi f t)], \quad (3)$$

where A is the actuation amplitude in the z-direction and f is the frequency of the sinusoidal function modulating the phase difference. In Eq. (3), when $A \geq \lambda/4$, the phase difference $\varphi(t)$ will sweep over the entire range of 2π in each cycle of the modulation, enabling both the maximum and minimum of I_{PD} to be measured in each modulation. In the experiment, we set $A = 0.5\ \mu m$, and the measured maximum and minimum values of I_{PD} during the sinusoidal modulation are:

$$I_1 = I_{PD,max} = I_R + I_S + 2\sqrt{I_R I_S}\gamma(z), \quad (4)$$

$$I_2 = I_{PD,min} = I_R + I_S - 2\sqrt{I_R I_S}\gamma(z). \quad (5)$$

Here, we assume that $\gamma(z)$ is unchanged during the modulation as the modulation amplitude is negligible compared to the coherence length of the light source. Combining Eqs. (4) and (5), with I_R being a known constant value measured prior to the experiment, the coherence function can be expressed as:

$$\gamma(z) = \frac{I_1 - I_2}{4\sqrt{I_R(\frac{I_1+I_2}{2} - I_R)}}. \quad (6)$$

Substituting Eq. (6) into Eq. (2), the coated layer surface position z can be derived.

To characterize the coherence function $\gamma(z)$ as a function of z, we replaced the coated layer with a flat mirror in the sample arm and focused the sample beam on this mirror surface. The optical path lengths of the sample and reference arms matched at $z = 0$. We used a motorized z-stage (Thorlabs, MLJ150/M) to shift the sample mirror in the z-direction with a step of 5 μm for a range of 600 μm. The sample beam intensity, $I_S = \frac{I_1+I_2}{2} - I_R$, as a function of z, is shown in Fig. 2(a), with the blue dots being the measured sample beam intensity and the red curve a Gaussian fitting. The peak in Fig. 2(a) represents the location of the focal plane. Figure 2(b) shows the characterization of the coherence function along the z-direction. The blue dots are the measured coherence function amplitudes using Eq. (6) and the red curve is a Gaussian fitting using the data within 250 μm from the matched path length. Note that the data at the two ends of Fig. 2(b) were excluded from the fitting, as the accuracy of the coherence function measurement was low due to low I_S. The FWHM of the fitted Gaussian curve in Fig. 2(b) is 360 μm, which is close to the theoretical value of 340 μm calculated from Eq. (2), confirming that the Gaussian-spectrum light source is a close estimation. In the experiment, we measured $\gamma(z)$ and derived the coated layer surface position z using the fitted Gaussian curve in Fig. 2(b). The displacement sensitivity of this technique was characterized to be 0.44 μm by continuously acquiring data at $z = 0$ and calculating the standard deviation of 500 depth measurements.

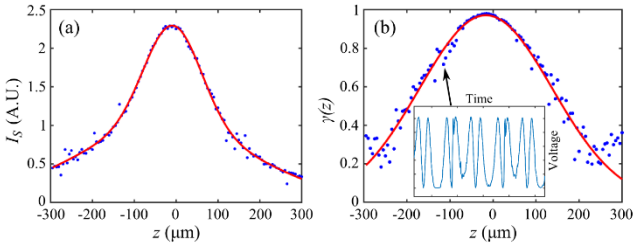

Fig. 2. Characterization of (a) sample arm intensity and (b) coherence function as a function of z. Each point in (b) is calculated from photodiode data over a period of 5 phase modulations. The inset in (b) is an example of raw data recorded by the photodiode.

We have verified CFE-OP on a tissue-mimicking silicone phantom with an embedded stiff inclusion and compared the results with OCT-based optical palpation. The bulk material of the phantom is a 5-mm thick, soft silicone compound (Wacker P7676 A and B at 1:1 mixing ratio) and the stiff inclusion is a 5 × 5 × 2 mm^3 silicone compound (Wacker RT601 A and B and silicone oil (Wacker, AK 50) at 10:1:10 mixing ratio) embedded 500 μm below the phantom surface. We placed the inclusion phantom on a motorized z-stage and added the multi-sectional compliant layer on top of the phantom. We raised the z-stage until the top surface of the compliant layer fully contacted with the imaging window and further raised the z-stage by ~2 mm to compress the layer and phantom. Figure 3(a) shows a photograph of the coated layer surface acquired using a digital camera when the layer is compressed. The shape of the inclusion can be identified from the contrast of the photograph. As a reference, an OCT scan of 400 × 400 pixels in x and y directions was performed on this phantom. Figure 3(b) is an OCT cross-sectional B-scan acquired on the location marked by the dashed red line in Fig. 3(a) after compression was applied. Upon compression, the coated layer surface deformed due to variation in mechanical properties in the phantom and is clearly seen as the bright curve in this figure. In OCT-based optical palpation, a Canny edge detection algorithm [5] was used to find the depth indices of the bright layer interface in each B-scan. From this OCT image, we note that the coating surface

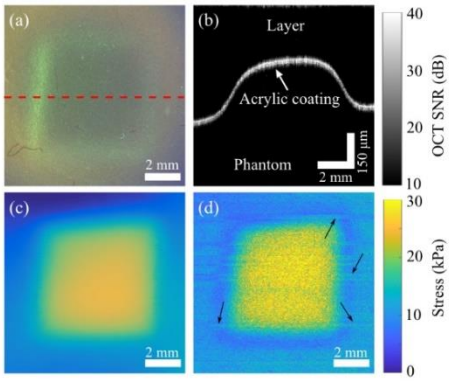

Fig. 3. (a) Photograph of the coated layer surface under compression against the inclusion phantom. (b) An OCT B-scan of the layer after compression is applied, acquired at the location marked by the red dashed line in (a). (c) and (d) Stress maps of the coated surface generated from OCT-based optical palpation and CFE-OP, respectively.

provides a strong reflection (>99%) with minimum light propagating to the tissue. The coating thickness was measured to be 20 μm. Figure 3(c) shows a 2-D stress map of the layer surface generated using OCT-based optical palpation. Then, we performed CFE-OP on this phantom at the same strain by scanning the beam in lateral directions with 400 × 400 pixels. A 2-D stress map was generated by combining the coherence function-encoded depth sensing and the stress-displacement curve Fig. 1(c), as shown in Figure 3(d). Comparing Figs. 3(c) and 3(d), they display similar stress values for the inclusion and bulk material. The stress map acquired with OCT is smoother due to the largely smoothed Canny edge detection algorithm, while CFE-OP does not require any smoothing and averaging in lateral directions in post-processing. The salt-and-pepper noise displayed in Fig. 3(d) and the horizontal lines indicated by the black arrows are imaging artefacts caused by unevenness of the coating on the layer surface. This can be improved in future works by using physical vapor deposition techniques for coating the layer surface. The low stress regions displayed near the inlcusion boundary are caused by low sample beam intensity I_S reflected off the sloped layer surface. This image artefact happens when the sample has large variations in mechanical properties. From our previous work on OCT-based optical palpation, we expect less mechanical contrast from tissue results. To minimize this image artefact in future, the beam intensity in the sample arm could be increased and a photodiode with a higher dynamic range used to avoid saturation.

We also performed CFE-OP on human breast tissue excised during a mastectomy procedure. This study was approved by the Sir Charles Gairdner and Osborne Park Health Care Group Human Research Ethics Committee (HREC No: 2007-152). The specimen was acquired immediately after the surgery, and a sample with dimensions of 30 × 40 × 5 mm^3 was dissected from the specimen. After the specimen was imaged, it was bisected and placed in two separate cassettes for histological processing. Figure 4(a) displays the photograph of the excised tissue specimen. Figure 4(b) displays the post-operative histology of the specimen, combining the histology prepared from the two separate cassettes. In Fig. 4(b), adipose tissue (A), fibrous tissue (F) and invasive ductal carcinoma (IDC) are identified from a histological assessment performed by a pathologist. For the CFE-OP measurement, the fresh tissue specimen was placed on a motorized *z*-stage and covered by the multi-sectional layer. The specimen was raised by the *z*-stage until the layer surface fully contacted with the imaging window and was further raised by ~1.5 mm to provide sufficient compression to the specimen. A 2-D stress map of the specimen was generated, as shown in Fig. 4(c). Figure 4(c) represents the tissue region outlined by the green frames in Figs. 4(a) and 4(b), confirmed by comparing the contrast in the photographs acquired with and without the compliant layer placed on top of the tissue. In Fig. 4(c), high stress values correspond to regions of IDC and low stress values correspond to adipose tissue and fibrous tissue. The shape of the tumor is clearly identified in Fig. 4(c), which is consistent with that assessed from the histology image Fig. 4(b).

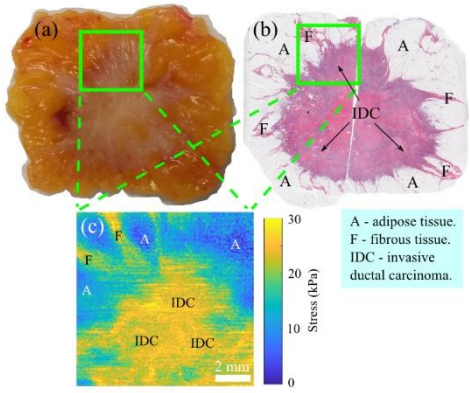

Fig. 4. (a) Photograph of the human breast tissue excised from a mastectomy specimen. (b) Histology of the tissue specimen. (c) Stress map generated from CFE-OP for the framed region in (a) and (b).

In this proof-of-principle study, we have demonstrated a maximum ~300 μm in depth sensing, limited by the coherence length of the laser source. To improve the mechanical contrast in images, we can add a band pass filter to the laser source to increase the coherence length, enabling the detection of higher strain imparted to the layer. We have achieved an acquisition rate of 400 Hz for each scan position, while the total scanning time for a 2-D stress map was approximately 7 minutes. The acquisition rate was limited by the piezoelectric actuator, however, reference phase modulation can be achieved using inertia-free devices, such as an electro optic modulator, which can readily extend the acquisition rate to the MHz regime. Alternatively, a 2-D array of charged coupled device can be used as the detector to acquire 2-D stress maps in a single shot without scanning the beam, significantly reducing the total time required for imaging the entire tissue surface. In addition to be applied in optical palpation, our coherence function-encoded depth sensing technique can also be used in profilometry for highly reflective surfaces.

In this Letter, we have introduced a simple, cost-effective optical palpation technique for 2-D stress mapping. We have performed CFE-OP on a silicone phantom and freshly excised human breast tissue, demonstrating comparable mechanical contrast to OCT-based optical palpation. Combined with the capability to be further realized in a more compact format using fiber optical components, CFE-OP holds promise for clinical applications, such as tumor margin assessment and scar treatment assessment.

Funding. Australian Research Council, the National Health and Medical Research Council (Australia), OncoRes Medical, Australia.

Disclosures. BFK (F, I), BL (I), CMS (I): OncoRes Medical.

References

1. K. M. Kennedy, S. Es'haghian, L. Chin, R. A. McLaughlin, D. D. Sampson, and B. F. Kennedy, Optical palpation: optical coherence tomography-based tactile imaging using a compliant sensor, Opt. Lett. **39**, 3014-3017 (2014).
2. W. M. Allen, P. Wijesinghe, B. F. Dessauvagie, B. Latham, C. M. Saunders, and B. F. Kennedy, Optical palpation for the visualization of tumor in human breast tissue, J. Biophotonics **12**, e201800180 (2019).
3. S. Es'haghian, K. M. Kennedy, P. Gong, D. D. Sampson, R. A. McLaughlin, and B. F. Kennedy, Optical palpation in vivo: imaging human skin lesions using mechanical contrast, J. Biomed. Opt. **20**, 16013 (2015).
4. R. W. Sanderson, Q. Fang, A. Curatolo, W. Adams, D. D. Lakhiani, H. M. Ismail, K. Y. Foo, B. F. Dessauvagie, B. Latham, C. Yeomans, C. M. Saunders, and B. F. Kennedy, Camera-based optical palpation, Sci. Rep **10**, 15951 (2020).
5. R. W. Sanderson, Q. Fang, A. Curatolo, A. Taba, H. M. DeJong, F. M. Wood, and B. F. Kennedy, Smartphone-based optical palpation: towards elastography of skin for telehealth applications, accepted by Biomed. Opt. Express.

6. B. Krajancich, A. Curatolo, Q. Fang, R. Zilkens, B. F. Dessauvagie, C. M. Saunders, and B. F. Kennedy, Handheld optical palpation of turbid tissue with motion-artifact correction, Biomed. Opt. Express **10**, 226-241 (2019).
7. B. S. Lee and T. C. Strand, Profilometry with a coherence scanning microscope, Appl. Opt. **29**, 3784-3788 (1990).
8. T. Dresel, G. Häusler, and H. Venzke, Three-dimensional sensing of rough surfaces by coherence radar, Appl. Opt. **31**, 919-925 (1992).
9. G. Häusler and M. W. Lindner, "Coherence radar" and "spectral radar"-new tools for dermatological diagnosis, J. Biomed. Optics **3**, 21-31 (1998).
10. P. Hariharan and M. Roy, White-light Phase-stepping Interferometry for Surface Profiling, J. Mod. Opt. **41**, 2197-2201 (1994).
11. C. Akcay, P. Parrein, and J. P. Rolland, Estimation of longitudinal resolution in optical coherence imaging, Appl. Opt. **41**, 5256-5262 (2002).